Movahedi, Nima; Vesenjak, Matej; Krstulovic-Opara, Lovre; Belova, Irina V.; Murch, Graeme E.; Fiedler, Thomas. “Dynamic compression of functionally-graded metal syntactic foams”. *Composite Structures* Vol. 261, no. 113308 (2021).

Available from: http://dx.doi.org/10.1016/j.compstruct.2020.113308

Dynamic Compression of Functionally-Graded Metal Syntactic Foams

Nima Movahedi [a], Matej Vesenjak [b], Lovre Krstulović-Opara [c],

Irina V. Belova [a], Graeme E. Murch [a], Thomas Fiedler [a]

[a] Centre for Mass and Thermal Transport in Engineering Materials, Discipline of Mechanical Engineering, School of Engineering, The University of Newcastle Australia, University Drive, Callaghan, NSW 2308, Australia

[b] Faculty of Mechanical Engineering, University of Maribor, Smetanova 17, 2000, Maribor, Slovenia.

[c] Faculty of Electrical Engineering, Mechanical Engineering and Naval Architecture, University of Split, R. Boškovića 32, 21000, Split, Croatia

Abstract

This study addresses the dynamic compression of functionally-graded (FG) metal syntactic foams (MSF). Cylindrical MSFs are manufactured by combining a ZA27 alloy with equal sized layers of expanded perlite (EP) and activated carbon (AC) particles. For comparison, uniform MSFs containing either particle type are manufactured with different aspect ratios. Samples are tested at the loading velocities 0.2 mm·s^{-1} (quasi-static) or 284 mm·s^{-1} (dynamic) to probe for changes of the deformation mechanism and effective mechanical properties. It is shown that uniform MSFs with a lower aspect ratio exhibit an increased overall strength. The underlying mechanism is a change of the shear failure mode, which has been closely studied by combining infrared (IR) imaging with dynamic compression. EP-MSFs exhibit a strength reduction at the higher loading velocity whereas AC-MSFs show no significant change. The dynamic deformation of FG-MSFs originates in the weaker EP layer and thus closely resembles the deformation behavior of the EP-MSFs. At higher strains, the deformation transitions to the AC layer and the stress-strain response changes accordingly.

Keywords: Metal syntactic foam; Functionally-graded foam; Aspect ratio; Quasi-static and dynamic compression; Shear failure, Deformation mode.

1. Introduction

In functionally graded materials (FGMs), physical (e.g. mechanical, thermal) properties change throughout the structure. [1]. Different types of FGMs such as sandwich plates were numerically studied to explore their dynamic, free vibration and buckling responses [2-4]. For instance, the influence of the aspect ratio was investigated on the buckling responses of FG plates [4]. Numerical studies were also carried out to explore the bending and free vibration of functionally graded porous plates [5, 6]. Auxetic cellular structures with functionally graded geometry, obtained by shape optimization, were also proposed and tested numerically in [7]. Metal syntactic foams (MSFs) are an emerging group of metallic foams consisting of either hollow [8,9] or porous [10-13] particles embedded within a metallic matrix. Due to their porous structure, MSFs absorb considerable deformation energy when compressed [14,15], making them attractive for impact attenuation [16] and energy absorbing structures [17]. Functionally-graded metal syntactic foam (FG-MSF) is a relatively new type of MSF. The FG-MSF contains at least two layers with different particles [18,19] and/or varying particle packing densities [20].

The mechanical properties and deformation mechanisms of FG-MSF in *quasi-static* compression were investigated in [18-20]. This is the first paper to discuss the dynamic compression of FG-MSFs and the dynamic properties of uniform MSFs with different aspect ratios. However, the dynamic compression and shear loading of uniform metallic foams, a uniform MSF and other functionally-graded cellular structures have been previously investigated [21-28]. Fiedler *et al.* [28] studied the dynamic compression of an aluminum/expanded perlite (EP) syntactic foam. Their results indicate a positive strain rate sensitivity of the tested MSF. Moreover, it was suggested that a pressure build-up within the highly porous EP particles increased the compression resistance of the material at a higher loading velocity compared to a quasi-static loading. Zhang *et al.* [29] compared the quasi-static and dynamic compression of an aluminum/glass cenosphere MSF. They observed an increased peak strength, plateau stress and energy absorption for dynamic loading. In another study [30], a zinc alloy (ZA27) matrix was combined with either expanded perlite or expanded glass particles. Unlike the aforementioned studies, the dynamic compression of the MSF showed a decrease in mechanical properties (plateau stress and energy absorption) in comparison to quasi-static loading. This behavior was attributed to the embrittlement of the matrix alloy at increased loading velocities. Kiernan *et al.* [31] studied the dynamic compression of a FG foam model using the finite element method. It was found that the amplitude of stress wave was changed due to a variation of local foam density along the loading direction. He *et al.* [32] studied the dynamic compression of a FG closed-cell aluminum foam with changing pore size in the longitudinal direction of the samples. It was found that the plateau region of the FG structures was extended relative to the uniform foams, which is beneficial for controlled energy absorption. In [33] the dynamic loading of functionally-graded hollow spheres was analyzed numerically. The results indicated an optimum energy absorption of the structure when compressed from the higher density side.

The present study investigates the dynamic compression of a two-layered FG-MSF. Each layer corresponds to a uniform MSF containing only a single particle type embedded within a metallic ZA27 matrix. For comparison, both the FG-MSF and uniform MSF (designated EP-MSF and AC-MSF) are tested in quasi-static and dynamic compression. In the FG-MSF samples, the height/diameter aspect ratio of the individual layers is halved. Therefore, uniform samples with different aspect ratios were tested to further investigate the effect of the aspect ratio on the deformation mechanism and mechanical properties of MSF. FG-MSFs are considered for application as optimized energy absorbers for dynamic loads in transport (e.g. automotive and railway) and structural applications [34].

2. Materials and Methods

2.1. Samples Manufacturing

A counter-gravity infiltration casting technique was used to manufacture all MSF samples tested in this study [35]. The ZA27 alloy was used as the matrix material and contains $25-28$ wt% aluminum and 2 wt% copper (the balance is zinc) [36]. First, uniform samples containing either EP or AC particles (supplied by Australian Perlite Pty and Seachem®, respectively) were manufactured and are subsequently referred to as EP-MSF and AC-MSF. In addition, FG-MSFs were produced via the infiltration of ZA27 into two stacked layers containing EP and AC particles. These particle layers were of equal height in the longitudinal sample direction. Further manufacturing details of FG-MSF samples are described in a previous study [18]. After solidification, all samples were machined to a height $H \approx 30$ mm and a diameter $D \approx 20$ mm in order to obtain an aspect ratio (AR) close to 1.5. Six uniform samples of each group (i.e. EP-MSF and AC-MSF) were kept with AR $= {}^{H}/_{D} = 1.5$. In addition, uniform MSF with aspect ratios of 0.5 and 1 were obtained by bisecting the remaining samples into segments of 10 mm and 20 mm height. Following machining, all samples were T6 heat-treated to improve the ductility of the ZA27 matrix alloy [10, 37]. To this end, the samples were subjected to a solution treatment at

365 °C for 1 h followed by cold water quenching. Subsequent artificial aging was performed at 140 °C for 24 h. The samples were then cooled to room temperature under atmospheric conditions. For engineering applications, MSFs can be cast in larger blocks and machined to the desired geometry. Alternatively, MSFs may be cast in-situ to fill structural elements such as tubes [11].

2.2. Samples Characterization

2.2.1. Physical Properties

The density of all syntactic foam samples (ρ) was calculated using their mass (m_{SF}) and volume (V_{SF}) according to Eq. (1):

$$\rho = {}^{m_{\mathrm{SF}}}/_{V_{\mathrm{SF}}} \tag{1}$$

In a uniform MSF, the volume fraction of particles ($\phi_{\mathrm{P,i}}$) was estimated based on the particle density (ρ_{P}) and bulk density (ϕ_{B}) of the respective filler type:

$$\phi_{\mathrm{P,i}} = {}^{\rho_{\mathrm{B}}}/_{\rho_{\mathrm{P}}} \tag{2}$$

In a FG-MSF, the overall volume fraction of particles (ϕ_{P}) was estimated considering the volume fraction of each layer (ϕ_{i}), which was assumed to be $\phi_{\mathrm{i}} = 0.5$

$$\phi_{\mathrm{P}} = \sum \phi_{\mathrm{P,i}}.\phi_{\mathrm{i}} = 0.5 \cdot \left(\phi_{\mathrm{P,EP}} + \phi_{\mathrm{P,AC}}\right) \tag{3}$$

Samples were carefully machined at both ends to achieve an equal layer height (i.e. $\phi_{\mathrm{i}} = 0.5$); however, the visual localisation of the layer's interphase at the sample's surfaces introduces an inaccuracy (see e.g. Fig. 7c). Therefore, small deviations of the actual layer heights will decrease the accuracy for the subsequent calculations of the volume fractions.

The volume fraction of the matrix (ϕ_{M}) in the uniform samples was calculated using Eq. (4) [18]:

$$\phi_{\mathrm{M}} = \frac{m_{\mathrm{SF}} - {}^{m_{\mathrm{P}}}/_{\rho_{\mathrm{ZA27}}}}{V_{\mathrm{SF}}} \tag{4}$$

where m_{SF} and m_{P} are the sample mass and combined particle mass (EP or AC), respectively. The particle mass (m_{P}) in a uniform MSF was estimated using the bulk density of the corresponding particle type [18]:

$$m_{\mathrm{P}} = \rho_{\mathrm{B}} . V_{\mathrm{SF}} \tag{5}$$

The total particle mass in FG-MSF was obtained using:

$$m_{\mathrm{P}} = V_{\mathrm{SF}} \cdot \sum\left(\phi_{\mathrm{i}} . \phi_{\mathrm{P,i}} . \rho_{\mathrm{P,i}}\right) = 0.5 V_{\mathrm{SF}} \cdot \left(\rho_{\mathrm{B,EP}} + \rho_{\mathrm{B,AC}}\right) \tag{6}$$

where the subscript i indicates the properties of each layer. The volume fraction of the matrix (ϕ_{M}) in a FG-MSF was then calculated using Eq. (4).

In all samples, the combined volume fractions of all constituents must be unity. Therefore, the volume fraction of the voids can be calculated using [18]:

$$\phi_{\mathrm{V}} = 1 - \phi_{\mathrm{M}} + \phi_{\mathrm{P}} \tag{7}$$

The physical properties of EP-MSF and AC-MSF samples with different aspect ratios and physical properties of graded samples are shown in Table 1.

Table 1. Physical properties of MSF

			Height [mm]	Diameter [mm]	Mass [g]	Density [g·cm^{-3}]	ϕ_M [-]	ϕ_P [-]	ϕ_V [-]
EP-MSF	AR≈1.5	QS	30.12	20.02	18.56	1.96	0.37	0.56	0.07
			30.17	19.99	19.58	2.07	0.40	0.56	0.04
			30.09	19.99	20.08	2.12	0.41	0.56	0.03
		Dynamic	30.14	20.09	17.56	1.84	0.35	0.56	0.09
			30.19	20.16	17.42	1.81	0.34	0.56	0.10
			30.00	19.96	17.92	1.91	0.36	0.56	0.08
	AR≈1	Dynamic	19.04	20.05	11.77	1.96	0.37	0.56	0.07
			19.04	19.98	12.23	2.05	0.39	0.56	0.05
			18.90	20.00	11.49	1.94	0.37	0.56	0.07
	AR≈0.5	Dynamic	9.07	20.03	5.67	1.98	0.38	0.56	0.06
			9.08	19.92	5.62	1.99	0.38	0.56	0.06
			9.05	19.90	5.26	1.87	0.36	0.56	0.08
AC-MSF	AR≈1.5	QS	30.11	20.04	22.29	2.35	0.37	0.59	0.04
			29.97	20.04	21.80	2.31	0.36	0.59	0.05
			30.10	19.99	21.48	2.27	0.36	0.59	0.05
		Dynamic	30.15	20.07	20.76	2.18	0.34	0.59	0.07
			30.07	20.12	20.62	2.16	0.33	0.59	0.08
			30.19	20.15	20.47	2.13	0.33	0.59	0.08
	AR≈1	Dynamic	19.09	20.06	13.19	2.19	0.34	0.59	0.07
			19.11	20.18	13.38	2.19	0.34	0.59	0.07
			19.07	20.06	13.37	2.22	0.35	0.59	0.06
	AR≈0.5	Dynamic	9.02	20.04	6.62	2.33	0.37	0.59	0.04
			9.06	20.07	6.20	2.17	0.34	0.59	0.07
			9.07	20.02	6.19	2.17	0.34	0.59	0.07
FG-MSF	AR≈1.5	QS	29.97	20.01	20.93	2.22	0.39	0.58	0.03
			30.30	20.05	20.64	2.17	0.37	0.58	0.05
			29.86	19.99	20.08	2.14	0.37	0.58	0.05
		Dynamic from EP layer	30.22	19.98	20.29	2.14	0.37	0.58	0.05
			30.28	20.24	18.99	1.95	0.33	0.58	0.09
			30.08	20.00	20.49	2.17	0.37	0.58	0.05
		Dynamic from AC Layer	30.21	20.02	19.46	2.05	0.35	0.58	0.07
			30.35	19.98	20.07	2.11	0.36	0.58	0.06
			30.00	19.91	20.20	2.16	0.37	0.58	0.05

2.2.2 Mechanical Properties

The compressive properties of the samples were characterized using a servo-hydraulic dynamic INSTRON 8801 testing machine. The crosshead displacement velocity was either 0.2 mm.s^{-1} (quasi-static) or 284 mm.s^{-1} (dynamic). Considering the average sample height, the higher loading velocity corresponds to engineering strain rates of 10 s^{-1}, 15 s^{-1} and 30 s^{-1} for MSFs with aspect ratios of 1.5, 1 and 0.5, respectively. Prior to compression, all samples were lubricated on both ends using the silicone-based MOLYKOTE 22 Medium lubricant. The force was measured using a 50 kN INSTRON DYNACELL load cell and logged alongside time and the machine crosshead displacement at a sampling rate of 5000 Hz. The corresponding engineering stress (σ) and strain (ε) values were then calculated based on the initial sample dimensions. Compressive stress-strain curves of the samples in each group were obtained for comparison. The mechanical properties of the samples were derived from the stress-strain data according to ISO 13314 [38]. According to ISO 13314, the compressive proof strength is the compressive stress at 1% plastic deformation. The plateau stress is the arithmetic mean of stress between 20% and 40% of total strain. The volumetric energy absorption was calculated up to 50% total strain according to Eq. (8) below [38]. Graphically, this energy can be interpreted as the area under the stress-strain curve up to 50% of compressive strain:

$$W = \int_0^{0.5} \sigma \, d\varepsilon \tag{8}$$

Lastly, the energy absorption efficiency was obtained using Eq. (9) [38]:

$$\eta = {}^{W}\!/_{0.5 \cdot \sigma_{\max}}, \tag{9}$$

where $\sigma_{\max}$ is the maximum stress up to 50% of the macroscopic strain.

2.2.3. Deformation Mechanism

To examine the deformation of the samples undergoing dynamic compression, infrared (IR) thermography imaging was conducted using a Flir SC 5000 high speed cooled middle-wave InSb detector camera [39]. A frequency of 320 Hz was employed to capture the plastic deformation of sample surfaces under dynamic loading. Due to rapid heat dissipation, IR imaging could not be used in case of quasi-static compression tests. The IR images were selected at constant time intervals to analyse the deformation mechanism of samples.

3. Results and Discussion

3.1. EP-MSF Samples

3.1.1. Physical Properties

The physical properties of all samples are shown in Table 1. The density of EP-MSF varies from 1.81 to 2.12 $g \cdot cm^{-3}$. A comparison between the physical properties of samples with different aspect ratios shows little deviation of the density and matrix volume fraction. As a result, any deviation of mechanical properties can be attributed to changes in the sample geometry and not density variations, which are well known to affect foam strength [40]. The EP-MSF samples used for quasi-static testing were manufactured in a second batch. It is evident that these samples exhibit a slightly higher average density compared to the dynamic samples. This is attributed to the wear of the graphite mold used for sample manufacturing.

3.1.2. Mechanical Properties

The compressive stress-strain curves of EP-MSFs are shown in Fig. 1. Density deviations between different EP-MSFs samples are relatively small (see Table. 1). Therefore, any deviation between their stress-strain curves is most likely due to their aspect ratios or loading velocity (see Fig. 1). The corresponding deformation mechanisms are detailed in the following section. Regardless of the sample aspect ratio and loading velocity, all curves exhibit the typical compressive stress-strain characteristics of cellular materials, i.e. initial linear elastic deformation followed by a stress plateau and eventually densification [41, 42]. Minor stress oscillations are observed in the plateau region of all EP-MSF samples. These are most likely related to the brittle deformation of the ZA27 matrix and the activation and arresting of shear bands. In addition to the individual curves, the average stress-strain curves of each group are plotted as bold lines for easier comparison. The morphology of the stress-strain curves changes with the aspect ratio of the samples in dynamic loading. EP-MSFs with the same aspect ratio exhibit almost identical compressive stress-strain curves; however, a distinct stress increase is visible for decreasing aspect ratios.

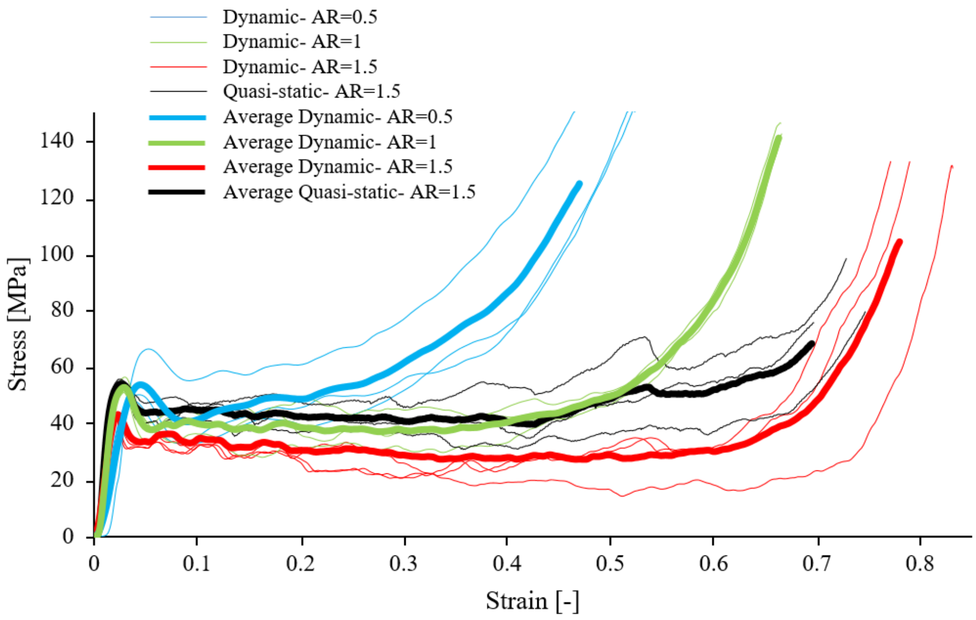

Fig. 1 Compressive stress-strain curves of EP-MSF samples with different aspect ratios under dynamic and quasi-static loading conditions

Following a linear quasi-elastic region, a stress drop is observed for all EP-MSF samples. In a previous study [10] it was shown that the stress drop is related to initiation of shear bands (cracks) during compression of MSFs. EP-MSFs with $H/D = 0.5$ uniquely exhibit strain hardening in their subsequent plastic plateau region. In contrast, an almost constant plateau stress is observed for the samples with the higher aspect ratios $H/D = 1, 1.5$. Moreover, increasing the aspect ratio of EP-MSF extends the plateau region to higher strain values and thus delays the onset of foam densification.

The compressive stress-strain curves of EP-MSFs with the aspect ratio 1.5 show a distinct deviation between quasi-static and dynamic loading. The quasi-static data exhibits higher stresses with a near constant stress offset at all strains. This deviation may be partially explained by the higher average density of the quasi-static EP-MSF samples (see Table 1). However, two samples exhibit similar densities (quasi-static: 1.96 g·cm^{-3} and dynamic: 1.91 g·cm^{-3}) and a clear stress deviation remains that can thus not be attributed to density variation alone. The contribution of the expanded perlite particles to the deformation of EP-MSFs (either in quasi-static or dynamic loading) is considered negligible due to the low strength of these particles. Hence, foam deformation is almost exclusively controlled by the ZA27 matrix material [18]. In a previous study, a negative strain rate sensitivity of ZA27 alloy was observed [30]. This negative strain rate sensitivity is attributed to an increasing brittleness of the zinc alloy with increasing deformation rate due to its HCP crystal structure [43, 44] and explains the lower strength of EP-MSF for dynamic compression. Interestingly, this behavior differs from A356 aluminum EP-MSF where a positive strain rate sensitive was observed instead [28].

3.1.3. Deformation Mechanism

The deformation of EP-MSF under dynamic loading is visualized in the IR images shown below (see Figs. 2a-c). In all samples, shear bands with an angle of $40 - 45°$ relative to the loading direction emerge during early deformation (see dashed rectangles in Figs. 2a-c). As described in section 3.1.2, the stress-strain curves of EP-MSF exhibit an initial stress drop that can be related to the activation of these shear bands. Further compression of the samples results in growth of the shear bands and eventually shear fracture (see Fig. 2a-c).

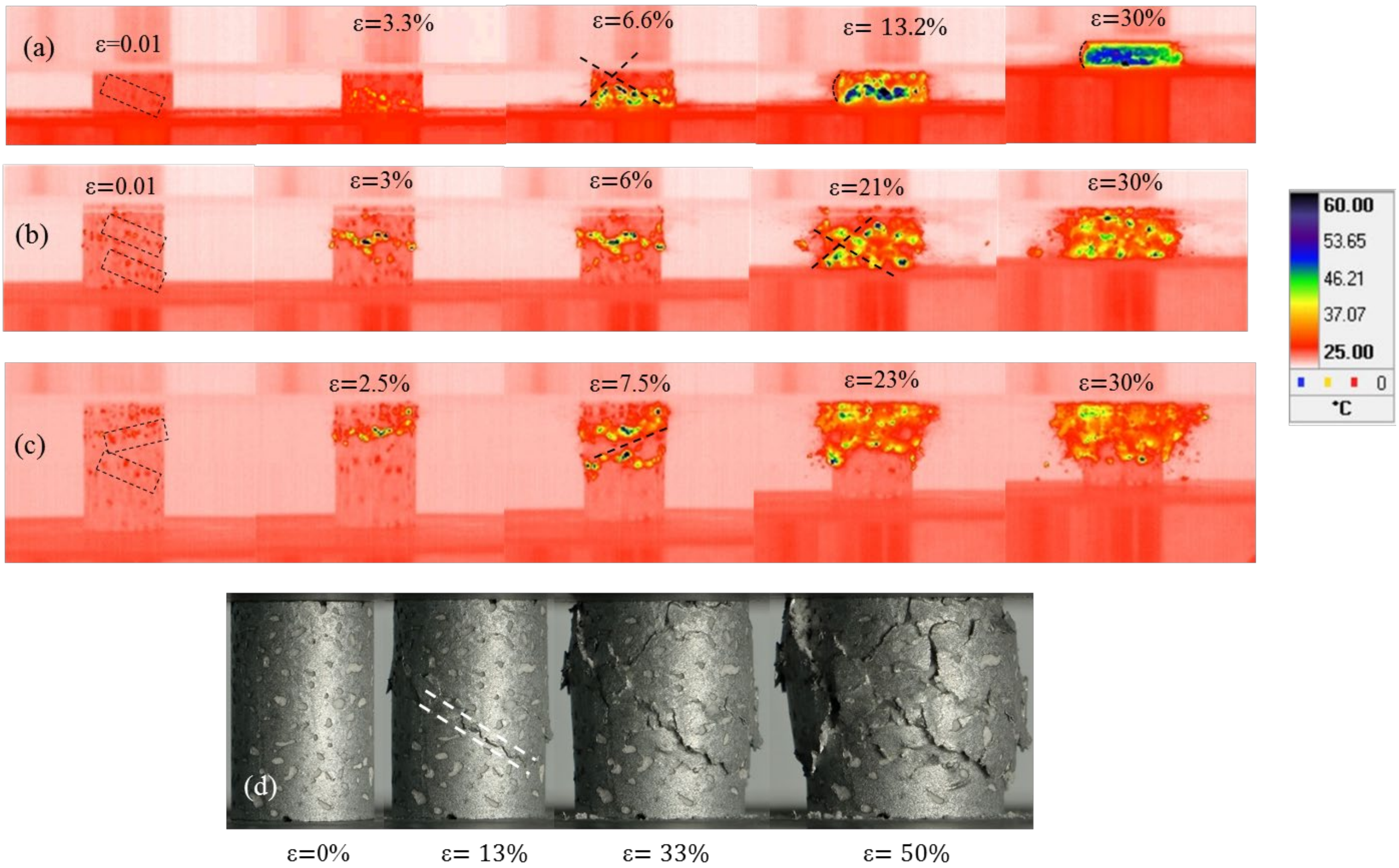

Fig. 2 Deformation of EP-MSF samples with different aspect ratios for dynamic loading (a) $H/_D = 0.5$, (b) $H/_D = 1$ and (c) $H/_D = 1.5$. and (d) $H/_D = 1.5$ (quasi-static loading).

The aspect ratio of a sample clearly affects its stress-strain response and deformation mechanism. In EP-MSFs with $H/_D = 0.5$, the $40 - 45°$ shear bands cannot geometrically bisect the samples across their vertical surfaces (see Fig. 3). As a result, the sample cannot compress via lateral motion and consequently plastic deformation with barreling is observed instead (see also Fig. 2 a). Following shear fracture, the larger sample fragment must still undergo plastic deformation, which becomes visible as increased temperatures across most of the sample surface in the IR imaging. This ongoing plastic deformation results in a decreased stress drop following shear fracture and strain hardening within the stress plateau. In EP-MSFs with $H/_D = 1$, shear bands with an orientation of 40° can bisect two vertical sample surfaces. The probability for this event is relatively low and most shear bands will instead cross one horizontal surface resulting in a similar deformation behavior to $H/_D = 0.5$. However, if the sample has been vertically separated (see the red shear band in Fig. 3) the deformation mechanism changes. Fragments shift laterally to permit the overall compression of the sample thus decreasing plastic deformation. This lateral motion requires less energy (and thus force) because plastic deformation and friction are mostly limited to the vicinity of the activated shear band. This lateral motion along shear bands is visible in both the dynamic IR images and quasi-static light photography (see Fig. 2). For the highest aspect ratio $H/_D = 1.5$, shear bands are more likely to intersect only vertical surfaces thus explaining the higher observed stress drop and lower plateau stress.

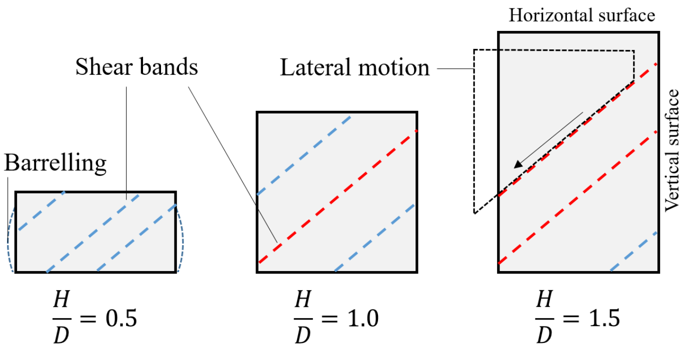

Fig.3 Schematic of EP-MSF deformation with different aspect ratios under dynamic loading.

No significant change of the deformation mechanism has been observed for quasi-static and dynamic loading of samples with $H/_D = 1.5$.

3.2. AC-MSF Samples

3.2.1. Physical Properties

The physical properties of AC-MSF samples are shown in Table 1. Like EP-MSF, low scattering of the AC-MSF samples with a similar aspect ratio is observed. An overall comparison shows that the volume fraction of AC-MSF constituents ($\phi_{M,}\phi_{P}, \phi_{V}$) falls within a narrow band for all samples. This ensures that the mechanical properties and deformation mechanism of AC-MSFs are influenced by their different aspect ratios and loading velocities rather than their composition. Analogous to EP-MSF, the AC-MSF samples used for quasi-static testing were manufactured in a second batch and exhibit a slightly increased density.

3.2.2. Mechanical Properties

The compressive stress-strain curves of AC-MSF are shown in Fig. 4. Unfortunately, the overload protection of the testing machine was triggered for the AC-MSF samples with an aspect ratio of 0.5 and the data is hence incomplete. All samples exhibit an initial stress peak that is followed by a significant rapid decline. Compared to the stress-strain curves of EP-MSF (see Fig. 1), the observed stress drop is significantly larger. The AC particles possess a much higher compressive strength compared to EP particles [18]. This is reflected in an increased peak stress of AC-MSF compared to EP-MSF. It was shown in [12] that stronger particles promote shear fracture in metal syntactic foams. The large observed stress drop is thus likely related to the partial failure of the strong AC particles followed by the formation of a catastrophic shear band through the brittle ZA27 matrix. Due to the same mechanism already described for EP-MSF, increasing the aspect ratio decreases the overall foam strength, especially for strains $\varepsilon < 0.3$. Samples with a higher aspect ratio eventually stabilize towards a stress plateau before undergoing densification at large strains.

Interestingly, the stress-strain curves of AC-MSF with an aspect ratio of 1.5 show little deviation irrespective of quasi-static and dynamic compression. This is contrary to the results observed for EP-MSF where the increasing brittleness of ZA27 under dynamic loading conditions [30] decreased the foam strength. A likely explanation for this discrepancy is the significantly higher strength of the AC particles, which thus contribute to the initial AC-MSF strength. Apparently, the AC particle strength is unaffected by the selected testing velocities and hence no clear deviation of the initial AC-MSF peak stress is found. However, the stress decline of the quasi-static samples has a decreased slope. The likely explanation is the increased brittleness of the ZA27 matrix for dynamic loading, which promotes the formation of shear bands [12] and thus accelerates the stress decline.

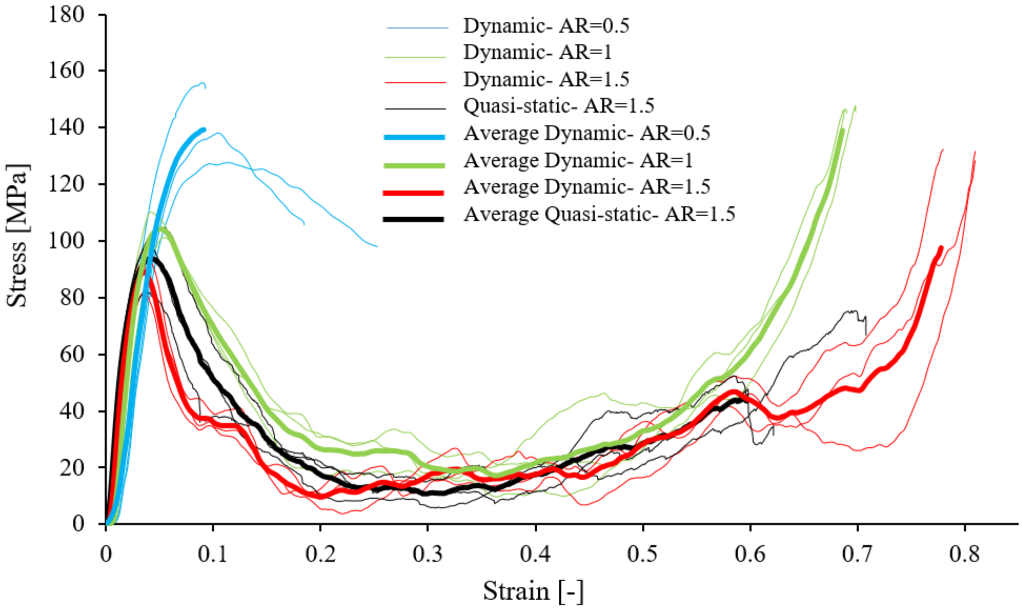

Fig. 4 Compressive stress-strain curves of AC-MSF samples with different aspect ratios under dynamic and quasi-static loading conditions.

3.2.3. Deformation Mechanism

The deformation of the AC-MSF samples is shown in Fig.5. All samples form shear bands resulting generally in sample fragmentation. However, AC-MSFs with an $H/_D = 0.5$ remains mostly intact without severe fragmentation, and barreling can be observed instead (see Fig. 5a). This deformation behavior resembles the EP-MSF samples of the same aspect ratio. The increased plastic deformation further explains the decreased stress drop (see Fig. 4) of AC-MSFs with AR $=$ 0.5 compared to the other samples. The deformation mechanism of AC-MSF with $H/_D \geq 1.0$ closely resembles EP-MSF, i.e. shear fracture is followed by the lateral motion of fragments. For $H/_D = 1$, multiple crossed shear bands emerge at low compressive strains (see Fig. 5b at $\varepsilon =$ 6.8%). Upon further compression, shear fracture eventually results in the fragmentation of the sample (see the dashed circle in Fig. 5b at $\varepsilon \approx 17\%$). The dynamic compression of AC-MSF with $H/_D = 1.5$ results in the formation of a major shear band with an angle of ~45° relative to the loading direction and the subsequent deformation of the sample occurs predominantly by lateral motion along this major shear band.

The quasi-static deformation of an AC-MSF sample with an aspect ratio 1.5 is shown in Fig. 5d. As in dynamic loading, compression is controlled by the lateral motion of partially connected sample fragments across major shear bands.

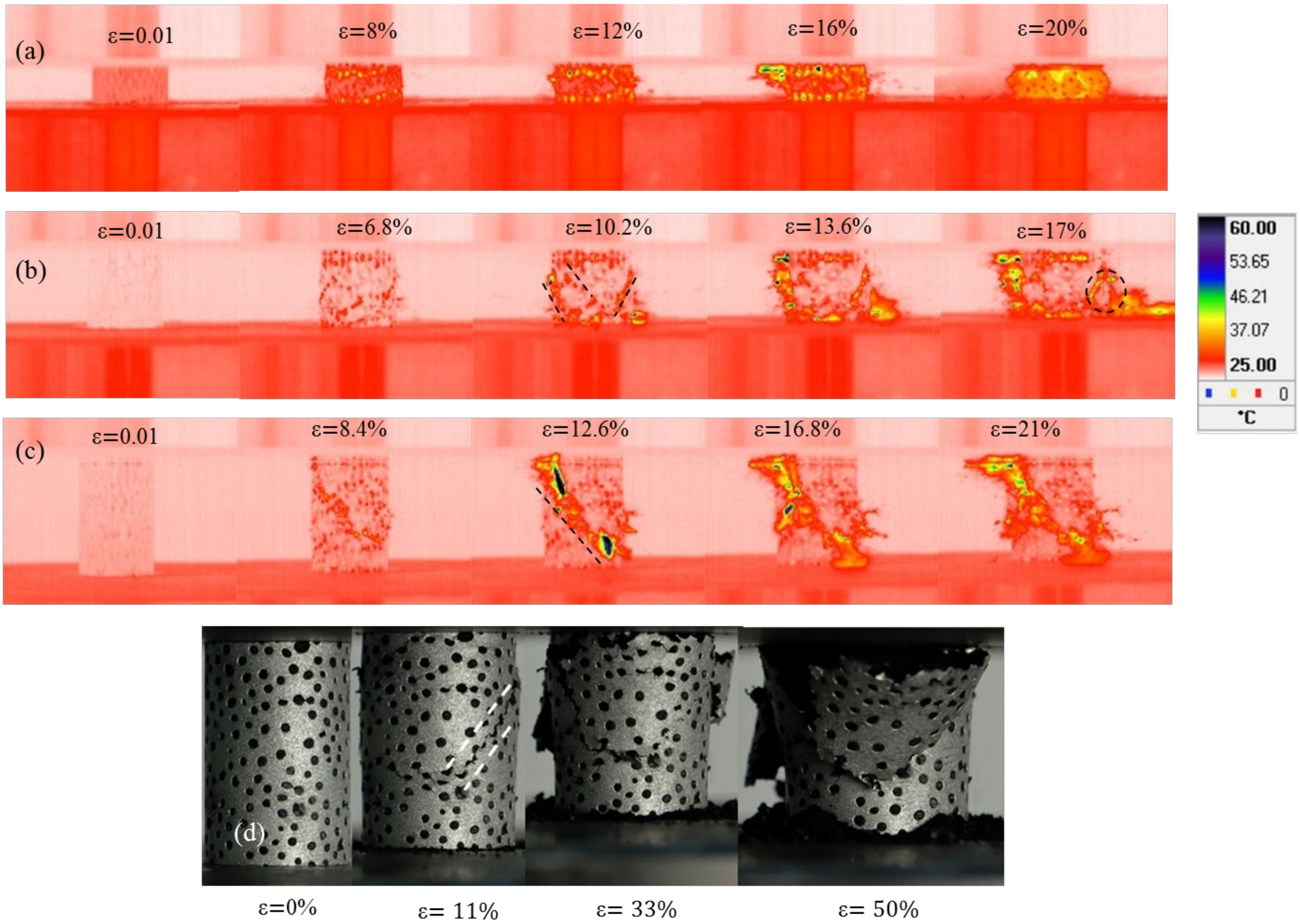

Fig. 5 Deformation of AC-MSF samples with different aspect ratios for dynamic loading (a) $H/_D = 0.5$, (b) $H/_D = 1$ and (c) $H/_D = 1.5$. and (d) $H/_D = 1.5$ (quasi-static loading).

3.3. FG-MSF Samples

3.3.1. Physical Properties

All FG-MSF samples were manufactured with the aspect ratio 1.5. As expected, the densities of the FG-MSF samples fall between the values of EP-MSFs and AC-MSFs (see Table 1). Analogous to the uniform MSF, the volume fractions of the matrix and voids in FG-MSFs exhibit only low scattering.

3.3.2. Mechanical Properties

The compressive stress-strain curves of FG-MSF are shown in Fig. 6. The different red line types represent dynamic loading from either the EP or the AC layer. It is apparaent that the stress-strain response is independent of the loading direction. This can be explained by the relatively low loading velocity which is four orders of magnitude below the sound velocity of the ZA27 alloy and allows the external load to be uniformly distributed within the material. Compared to the stress-strain data of EP-MSF and AC-MSF, the FG-MSF curves exhibit a distinctly higher scattering. A possible explanation are deviations in the layer heights that may reinforce the intrinsic strength variation of the metallic foams.

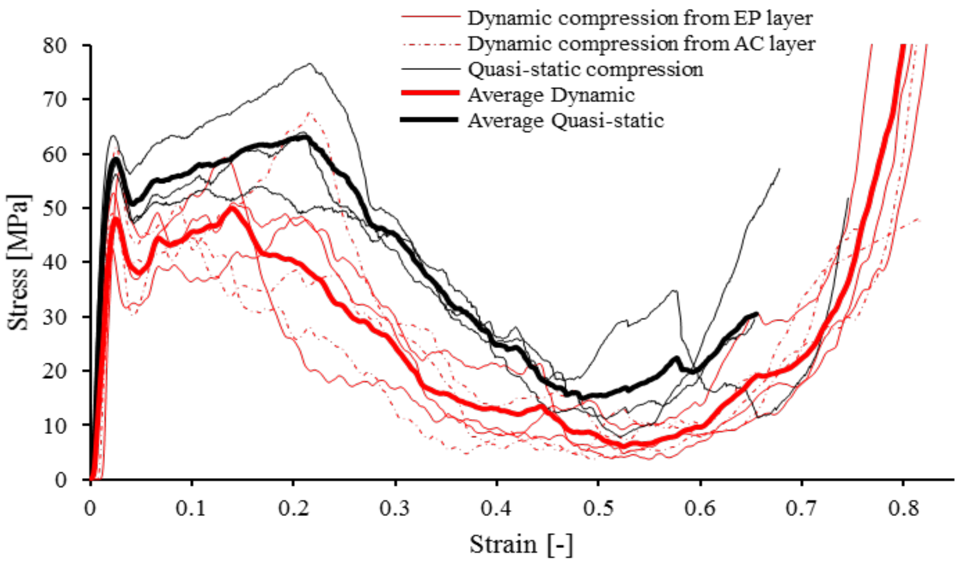

Fig. 6 Compressive stress-strain curves of FG-MSF samples under dynamic and quasi-static loading conditions.

The initial stress-strain response of FG-MSF resembles the data of EP-MSF (see Fig. 1). Similar to EP-MSF with $H/_D = 0.5$, an initial stress peak is followed by strain hardening behavior up to the emergence of a second peak. Following this second peak, the stress declines, now resembling the compression behavior of uniform AC-MSFs (see Fig. 4). It is worth highlighting that the second stress peak of FG-MSF does not reach the magnitude of AC-MSF. In summary, the stress-strain curves of FG-MSF are composed of two sections that can be related to the deformation of its individual layers. A similar behavior was observed for the quasi-static deformation of layered FG-MSF [18-20].

The comparison between the quasi-static and dynamic stress at low strains reveals a near constant offset analogous to EP-MSF. Thus, FG-MSF exhibits a higher strength for quasi-static compared to dynamic loading. Moreover, the second peak in quasi-static loading reaches higher stress values compared to dynamic loading. Once again, this can be explained by the decreased brittleness of the ZA27 alloy at lower loading velocities, which delays the onset of macroscopic shear failure.

3.3.3. Deformation Mechanism

Fig. 7 shows the deformation of FG-MSF loaded from the EP-layer (a) and the AC-layer (b). Regardless of loading direction, the dynamic deformation of FG-MSF is sequential, initiates within the weaker EP-layer, and only encompasses the stronger AC-layer at higher strains. The same deformation mechanism is observed for the quasi-static compression of FG-MSF shown in Fig. 7c.

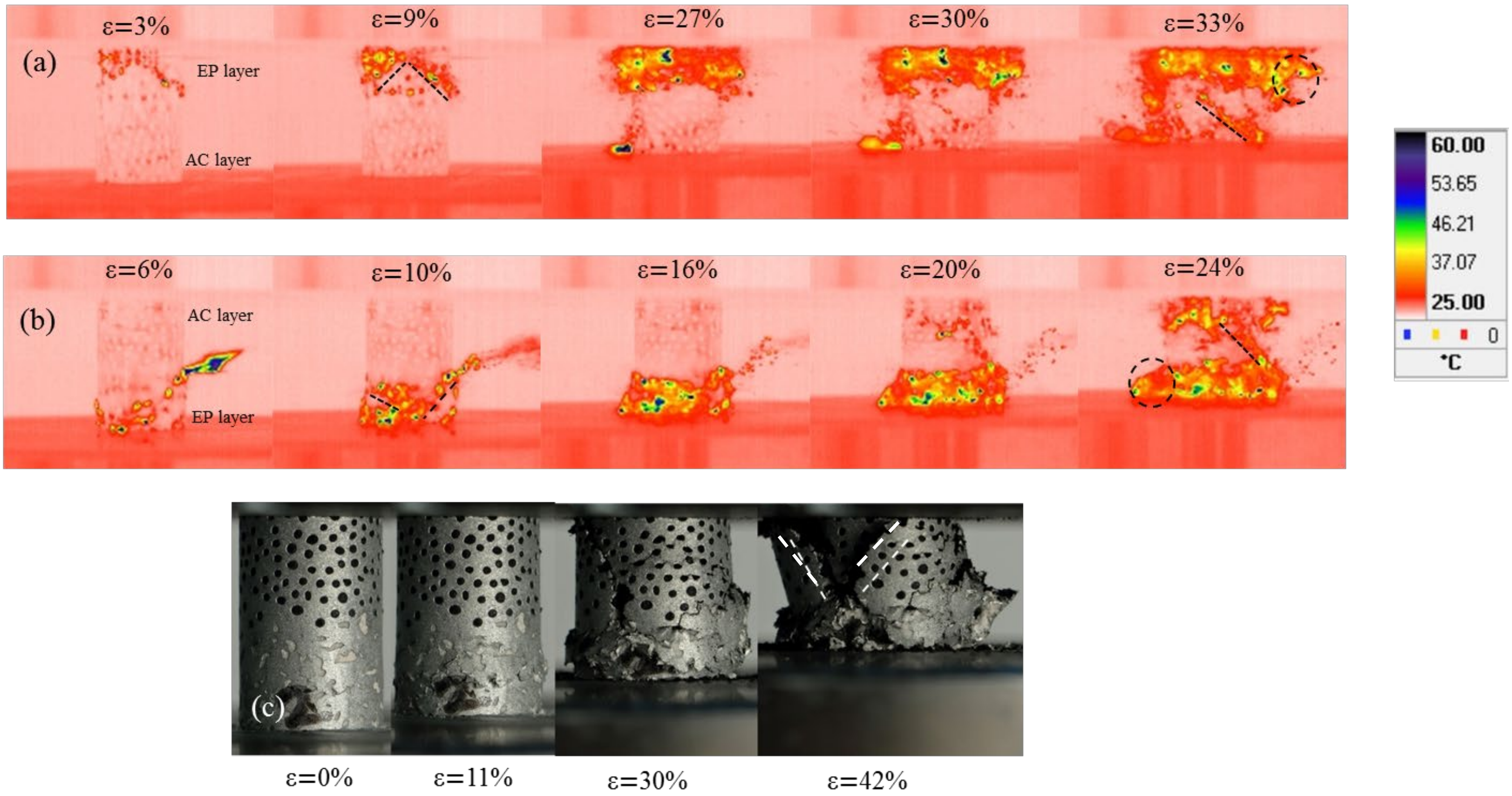

Fig.7 Deformation of FG-MSF samples loaded from (a) EP layer (b) AC layer and (c) quasi-static loading

A FG-MSF layer height of approximately 15 mm results in the layer aspect ratio 0.75. Therefore, a deformation behavior similar to uniform MSF with the aspect ratio 0.5 to 1.0 is expected. At low strain, the EP layer starts to compress and shear bands emerge. This is independent of the loading direction. Unlike the dynamic deformation of uniform EP-MSF with the aspect ratio 0.5 (see Fig. 2a), lateral motion of the EP layer occurs at higher strains (see dashed circles in Fig.7 a and b). Therefore, the deformation mechanism of the EP-layer more closely resembles the deformation of uniform EP-MSF with the aspect ratio 1 (see Fig. 2b). The subsequent deformation of the AC layer leads to the formation of a macroscopic shear band. Analogous to AC-MSF (see Fig.5b), the deformation of the AC-layer progresses by lateral motion along shear bands.

3.4. Effective Mechanical Properties

Fig. 8 shows the effective mechanical properties of EP-MSF, AC-MSF and FG-MSF. Data points are plotted versus the average sample density for the considered aspect ratios and dynamic and quasi-static compression.

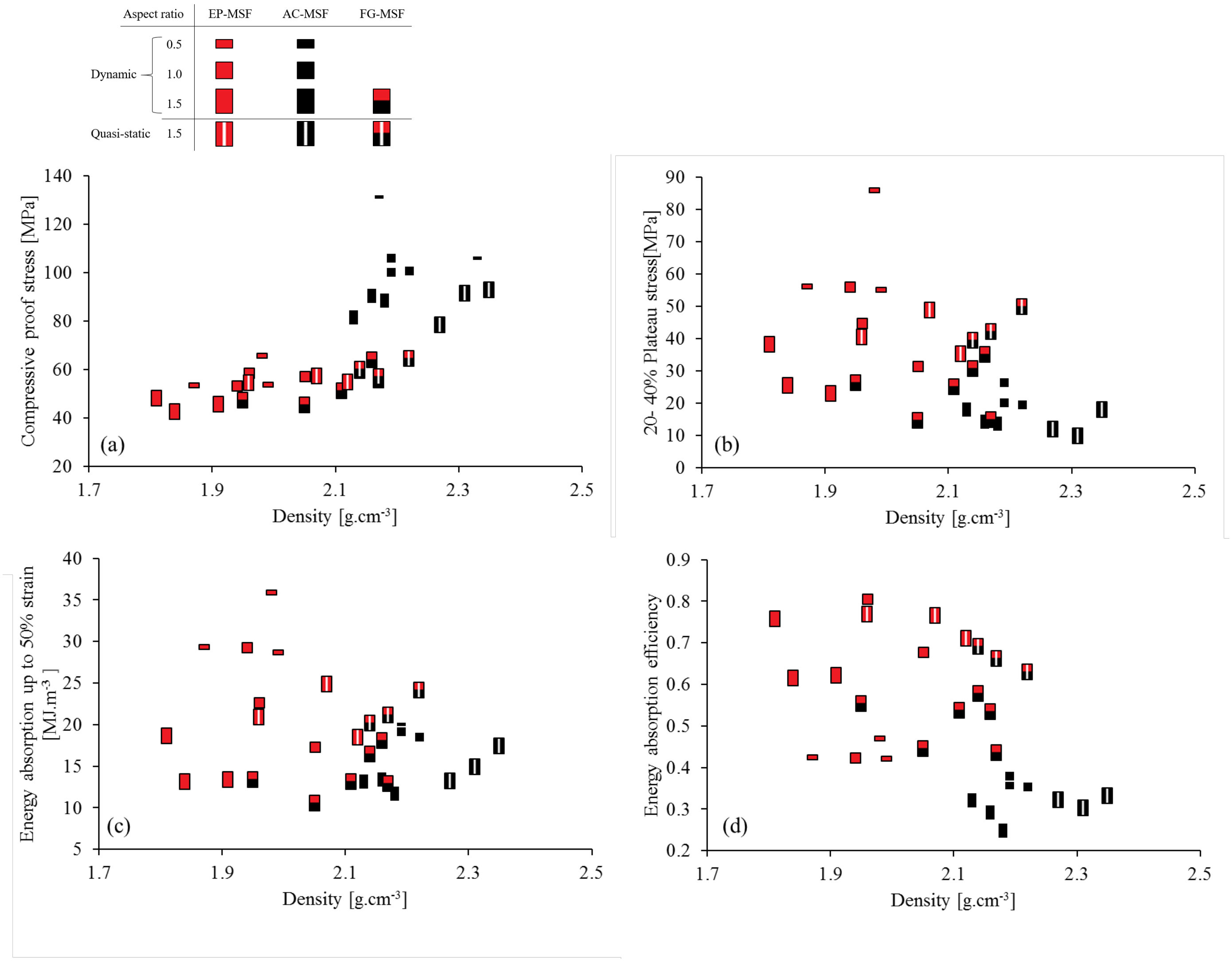

Fig. 8 Effective mechanical properties of EP-MSF, AC-MSF and FG-MSF.

Compressive Proof Stress

Fig. 8a shows the compressive proof stress plotted versus the average density. As an overall trend, the proof stress increases with the foam density. In the case of EP-MSF, only a minor increase of the proof stress is observed for smaller aspect ratios. This effect is distinctly more pronounced in the case of AC-MSF and is likely attributed to the earlier discussed differences in shear band propagation. AC-MSF exhibits a higher compressive proof stress compared to EP-MSF. Given similar ZA27 matrix volume fractions (see Table 1), this deviation can be attributed to the differing compressive strength of filler particles. In [18] it was shown that the compression of individual AC particles requires a considerably higher force compared to EP fillers. The compressive proof stress of FG-MSF is similar to the values of EP-MSF. As described in section 3.3, the initial deformation of FG-MSF is concentrated within the weaker EP layer and hence EP-MSF and FG-MSF share similar properties at 1% macroscopic compression.

Samples with the aspect ratio 1.5 were tested both at quasi-static and dynamic loading velocities. A slight increase of the proof stress can be found for quasi-static loading compared to dynamic compression. This may, at least in part, be attributed to a negative strain rate sensitivity of the ZA27 alloy [30, 44]. However, the quasi-static samples also exhibit slightly higher densities, which superimposes a possible minor dependency on the loading velocity.

Plateau Stress

The $20 - 40\%$ plateau stress of uniform and functionally-graded MSF is shown in Fig. 8b. Due to the premature termination during the compressive testing of AC-MSF with the aspect ratio 0.5, no plateau stresses could be obtained for these samples. A correlation between the aspect ratio of uniform MSF and their plateau stress can be observed. In particular, the plateau stress of EP-MSF exhibits a strong dependency on the aspect ratio. The plateau stress is defined as the stress average between $0.2 - 0.4$ of strain. This interval follows the initial stress drop in the stress-strain curves (shearing of the sample under compressive loading). Therefore, a likely explanation for the observed dependency of the plateau stress on the aspect ratio are the different shearing modes either suppressing or promoting lateral sample motion during compression (see Fig. 3). In EP-MSFs with the aspect ratio 0.5, sample fragments undergo significant plastic deformation (see Figs.2a and 3) resulting in a higher plateau stress. For higher aspect ratios (see corresponding IR Figs.2b and c), lateral sample motion is observed instead which requires lower forces resulting in a decreased plateau stress. AC-MSFs with the aspect ratio 1 and 1.5 exhibit similar shear fracture behavior (see Figs. 5b and c) and hence only a minor change in their plateau stress.

The effect of the loading velocity on the plateau stress of EP-MSF is apparent, i.e. the plateau stress under quasi-static loading is significantly higher compared to dynamic loading. Interestingly, the loading velocity does not appear to change the plateau stress of AC-MSF. A likely explanation is that the deformation of AC-MSFs is strongly affected by the strong AC particles. In contrast, the ZA27 matrix provides the structural support in EP-MSFs. As a result, the negative strain rate sensitivity of ZA27 [30, 44] becomes visible as a decreasing plateau stress in the case of dynamic compression. In addition, the higher densities of the quasi-static samples may contribute to this trend.

The plateau stress of FG-MSF is similar to EP-MSF. Albeit the compressive deformation reaches the AC layer at $20 - 30\%$ compression (see Figs. 6 and 7), most deformation remains concentrated within the EP layer. Following the trend of EP-MSF, FG-MSF also exhibits higher plateau stresses for quasi-static compression.

Volumetric Energy Absorption

The definition of the volumetric energy absorption resembles the plateau stress, i.e. it is mostly determined by the average stresses within a similar strain interval. As a result, the data points mirror the trends observed for the plateau stress (see Fig. 8c). Most importantly, the energy absorption of uniform MSF increases with decreasing aspect ratio and lower loading velocities. The maximum energy absorption is obtained for EP-MSF with the aspect ratio 0.5. The energy absorption of FG-MSF is similar to EP-MSF.

Energy Absorption Efficiency

The energy absorption efficiency is plotted in Fig. 8d. This property is a measure for stress variation within the stress plateau. A high efficiency corresponds to near constant plateau stresses, which is beneficial for impact attenuation. Globally, an opposing trend to the other material properties emerges, i.e. the efficiency appears to decrease with increasing density. Furthermore, the energy absorption of EP-MSF clearly exceeds the values obtained for AC-MSF. The maximum values are observed for EP-MSF with the aspect ratio 1.5. This is true for both quasi-static and dynamic compression. The high energy absorption efficiency of EP-MSF can be related to a uniform plateau stress (see Fig. 1). This stress-strain data further shows strain hardening for EP-MSF samples with the aspect ratio 0.5, which visibly decreases the corresponding energy absorption efficiency. The efficiency of AC-MSF is generally lower, which can be explained by the high peak stress that is followed by a significant stress drop towards the plateau (see Fig. 4).

The energy absorption efficiency of FG-MSF falls between the values of EP-MSF and AC-MSF. Whilst the initial deformation of these samples is dominated by the EP-MSF layer, the stress drop at the compressive strains $0.2 - 0.3$ negatively affects the efficiency. As a result, the samples are unable to reach the performance of EP-MSFs but outperform AC-MSFs.

No clear correlation between the loading velocity and the energy absorption efficiency of AC-MSF can be identified. In the case of EP-MSF and FG-MSF, the data suggests an increase of the efficiency for quasi-static compression. This can attributed to the decreased brittleness of the ZA27 alloy at lower loading velocities.

4. Conclusions

In the presented study, uniform and functionally-graded MSF were subjected to dynamic and quasi-static compression. The following conclusions can be drawn:

- The formation of shear bands was observed in all tests.
- At higher strains, most samples underwent shear fracture.
- IR imaging of samples with a low aspect ratio showed significant plastic deformation, even following shear fracture. In contrast, samples with a higher aspect ratio compressed via the lateral motion of sample fragments. In this case, plastic deformation was limited to the vicinity of shear sliding planes.
- Regardless of the loading direction, the dynamic deformation of FG-MSF commenced within the weaker EP layer. As a result, the initial deformation behavior closely resembled EP-MSF with the aspect ratio 1. At higher strains, the deformation transitioned to the AC layer.
- The deformation mechanism was not affected by the considered loading velocities.
- In all samples, increasing deformation velocity decreases the overall strength of the matrix material due to a negative strain rate sensitivity of the ZA27 alloy. This is visible in the properties of EP-MSF that tend to deteriorate with increasing loading velocity. However, the high strength AC particles partially suppress this effect in AC-MSF.
- AC-MSF exhibits the highest compressive proof stress. The compressive proof stress of FG-MSF is similar to EP-MSF. The proof stress of all sample types decreases with increasing aspect ratio.
- EP-MSF exhibits the highest plateau stress. The plateau stress of FG-MSF is similar to EP-MSF. The plateau stress of EP-MSF rapidly decreases with increasing aspect ratio. This trend is much weaker in the case of AC-MSF.
- Volumetric energy absorption follows the same trend as the plateau stress.

- EP-MSF exhibits the highest energy absorption efficiency. In comparison, the energy absorption efficiency of AC-MSF is significantly lower (almost 1/3). The energy absorption efficiency of FG-MSF falls between these groups.

References

[1] Mahamood RM, Akinlabi ET. Functionally Graded Materials: Springr, 2017.

[2] Menasria A, Kaci A, Bousahla AA, Bourada F, Tounsi A, Benrahou KH, et al. A four-unknown refined plate theory for dynamic analysis of FG-sandwich plates under various boundary conditions. Steel and Composite Structures. 2020;36:355-367. http://dx.doi.org/10.12989/scs.2020.36.3.355

[3] Rabhi M, Benrahou KH, Kaci A, Houari MSA, Bourada F, Bousahla AA, et al. A new innovative 3-unknowns HSDT for buckling and free vibration of exponentially graded sandwich plates resting on elastic foundations under various boundary conditions Geomechanics and Engineering. 2020;22:119-32. https://doi.org/10.12989/gae.2020.22.2.119

[4] Chikr SC, Kaci A, Bousahla AA, Bourada F, Tounsi A, Bedia EAA, et al. A novel four-unknown integral model for buckling response of FG sandwich plates resting on elastic foundations under various boundary conditions using Galerkin's approach Geomechanics and Engineering. 2020;21:471-87. https://doi.org/10.12989/gae.2020.21.5.471

[5] Zine A, Bousahla AA, Bourada F, Benrahou KH, Tounsi A, Adda Bedia EA, et al. Bending analysis of functionally graded porous plates via a refined shear deformation theory Computers and Concrete. 2020;26:63-74. http://dx.doi.org/10.12989/cac.2020.26.1.063

[6] Kaddari M, Kaci A, Bousahla AA, Tounsi A, Bourada F, Tounsi A, et al. A study on the structural behaviour of functionally graded porous plates on elastic foundation using a new quasi-3D model: Bending and free vibration analysis Computers and Concrete. 2020;25:37-57. https://doi.org/10.12989/cac.2020.25.1.037

[7] Novak N, Vesenjak M, Ren Z. Computational Simulation and Optimization of Functionally Graded Auxetic Structures Made From Inverted Tetrapods. physica status solidi (b). 2017;254. https://doi.org/10.1002/pssb.201600753

[8] Orbulov IN. Compressive properties of aluminium matrix syntactic foams. Mater. Sci. Eng. A. 2012;555:52-6. https://doi.org/10.1016/j.msea.2012.06.032

[9] Anbuchezhiyan G, Mohan B, Sathianarayanan D, Muthuramalingam T. Synthesis and characterization of hollow glass microspheres reinforced magnesium alloy matrix syntactic foam. J. Alloys Compd. 2017;719:125-32. https://doi.org/10.1016/j.jallcom.2017.05.153

[10] Movahedi N, Murch GE, Belova IV, Fiedler T. Effect of Heat Treatment on the Compressive Behavior of Zinc Alloy ZA27 Syntactic Foam. Materials (Basel). 2019;12. https://doi.org/10.3390/ma12050792

[11] Taherishargh M, Vesenjak M, Belova IV, Krstulović-Opara L, Murch GE, Fiedler T. In situ manufacturing and mechanical properties of syntactic foam filled tubes. Mater.Des. 2016;99:356-68. https://doi.org/10.1016/j.matdes.2016.03.077

[12] Al-Sahlani K, Kisi E, Fiedler T. Impact of particle strength and matrix ductility on the deformation mechanism of metallic syntactic foam. J. Alloys Compd. 2019;786:292-9. https://doi.org/10.1016/j.jallcom.2019.01.283

[13] Movahedi N, Taherishargh M, Belova IV, Murch GE, Fiedler T. Mechanical and Microstructural Characterization of an AZ91-Activated Carbon Syntactic Foam. Materials (Basel). 2018;12. https://doi.org/10.3390/ma12010003

[14] Szlancsik A, Katona B, Bobor K, Májlinger K, Orbulov IN. Compressive behaviour of aluminium matrix syntactic foams reinforced by iron hollow spheres. Mater. Des.2015;83:230-7. https://doi.org/10.1016/j.matdes.2015.06.011

[15] Linul E, Lell D, Movahedi N, Codrean C, Fiedler T. Compressive properties of zinc syntactic foams at elevated temperatures. Compos. B. Eng.2019;167:122-34. https://doi.org/10.1016/j.compositesb.2018.12.019

[16] Fiedler T, Taherishargh M. Large-scale drop test on perlite–metal syntactic foam. J. Compos. Mater.2018;53:515-20. https://doi.org/10.1177/0021998318786994

[17] Lehmhus D, Vesenjak M, Schampheleire S, Fiedler T. From Stochastic Foam to Designed Structure: Balancing Cost and Performance of Cellular Metals. Materials (Basel).2017;10. https://doi.org/10.3390/ma10080922

[18] Movahedi N, Murch GE, Belova IV, Fiedler T. Functionally graded metal syntactic foam: Fabrication and mechanical properties. Mater. Des. 2019;168. https://doi.org/10.1016/j.matdes.2019.107652

[19] Movahedi N, Conway S, Belova IV, Murch GE, Fiedler T. Influence of particle arrangement on the compression of functionally graded metal syntactic foams. Mater. Sci. Eng. A.2019;764. https://doi.org/10.1016/j.msea.2019.138242

[20] Fiedler T, Movahedi N, York L, Broxtermann S. Functionally-Graded Metallic Syntactic Foams Produced via Particle Pre-Compaction. Metals. 2020;10. https://doi.org/10.3390/met10030314

[21] Linul E, Marsavina L, Kováčik J. Collapse mechanisms of metal foam matrix composites under static and dynamic loading conditions. Mater. Sci. Eng. A. 2017;690:214-24. https://doi.org/10.1016/j.msea.2017.03.009

[22] Duarte I, Vesenjak M, Krstulović-Opara L, Ren Z. Static and dynamic axial crush performance of in-situ foam-filled tubes. Compos. Struct. 2015;124:128-39. https://doi.org/10.1016/j.compstruct.2015.01.014

[23] Sarıkaya M, Taşdemirci A, Güden M. Dynamic crushing behavior of a multilayer thin-walled aluminum corrugated core: The effect of velocity and imperfection. Thin-Walled Struct. 2018;132:332-49. https://doi.org/10.1016/j.tws.2018.06.029

[24] Novak N, Krstulović-Opara L, Ren Z, Vesenjak M. Compression and shear behaviour of graded chiral auxetic structures. Mech. Mater. 2020;148. https://doi.org/10.1016/j.mechmat.2020.103524

[25] Duarte I, Vesenjak M, Krstulović-Opara L, Ren Z. Crush performance of multifunctional hybrid foams based on an aluminium alloy open-cell foam skeleton. Polym. Test. 2018;67:246-56. https://doi.org/10.1016/j.polymertesting.2018.03.009

[26] Kılıçaslan C, Güden M, Odacı İK, Taşdemirci A. Experimental and numerical studies on the quasi-static and dynamic crushing responses of multi-layer trapezoidal aluminum corrugated sandwiches. Thin-Walled Struct. 2014;78:70-8. https://doi.org/10.1016/j.tws.2014.01.017

[27] Anantharaman H, Shunmugasamy VC, Strbik OM, Gupta N, Cho K. Dynamic properties of silicon carbide hollow particle filled magnesium alloy (AZ91D) matrix syntactic foams. Int. J. Impact Eng. 2015;82:14-24. https://doi.org/10.1016/j.ijimpeng.2015.04.008

[28] Fiedler T, Taherishargh M, Krstulović-Opara L, Vesenjak M. Dynamic compressive loading of expanded perlite/aluminum syntactic foam. Mater. Sci. Eng. A. 2015;626:296-304. https://doi.org/10.1016/j.msea.2014.12.032

[29] Zhang B, Lin Y, Li S, Zhai D, Wu G. Quasi-static and high strain rates compressive behavior of aluminum matrix syntactic foams. Compos. B. Eng. 2016;98:288-96. https://doi.org/10.1016/j.compositesb.2016.05.034

[30] Broxtermann S, Vesenjak M, Krstulović-Opara L, Fiedler T. Quasi static and dynamic compression of zinc syntactic foams. J. Alloys Compd. 2018;768:962-9. https://doi.org/10.1016/j.jallcom.2018.07.215

[31] Kiernan S, Cui L, Gilchrist MD. Propagation of a stress wave through a virtual functionally graded foam. Int J Non Linear Mech. 2009;44:456-68. https://doi.org/10.1016/j.ijnonlinmec.2009.02.006

[32] He S-Y, Zhang Y, Dai G, Jiang J-Q. Preparation of density-graded aluminum foam. Mater. Sci. Eng. A. 2014;618:496-9. https://doi.org/10.1016/j.msea.2014.08.087

[33] Fan J, Zhang J, Wang Z, Li Z, Zhao L. Dynamic crushing behavior of random and functionally graded metal hollow sphere foams. Mater. Sci. Eng. A. 2013;561:352-61. https://doi.org/10.1016/j.msea.2012.10.026

[34] Garcia-Moreno F. Commercial Applications of Metal Foams: Their Properties and Production. Materials (Basel). 2016;9. https://doi.org/10.3390/ma9020085

[35] Movahedi N, Murch GE, Belova IV, Fiedler T. Manufacturing and compressive properties of tube-filled metal syntactic foams. J. Alloys Compd. 2019.

https://doi.org/10.1016/j.jallcom.2019.153465

[36] ASTM B86-13. Standard specification for zinc and zinc-aluminum (ZA) alloy foundry and diecastings.

[37] Liu Y, Li H-y, Jiang H-f, Lu X-c. Effects of heat treatment on microstructure and mechanical properties of ZA27 alloy. Trans. Nonferrous Met. Soc. 2013;23:642-9. https://doi.org/10.1016/S1003-6326(13)62511-X

[38] ISO13314 Mechanical testing of metals - ductility testing - compression test for porous and cellular metals (2011) Switzerland.

[39] Krstulović-Opara L, Surjak M, Vesenjak M, Tonković Z, Kodvanj J, Domazet Ž. Comparison of infrared and 3D digital image correlation techniques applied for mechanical testing of materials. Infrared Phys. Technol. 2015;73:166-74. https://doi.org/10.1016/j.infrared.2015.09.014

[40] Gibson L.J, Ashby M.F. Cellular Solids: Structure and Properties, 2nd ed., Cambridge University Press, Cambridge, 1997.

[41] Movahedi N, Linul E. Mechanical properties of Light Expanded Clay Aggregated (LECA) filled tubes. Mater. Lett. 2018;217:194-7. https://doi.org/10.1016/j.matlet.2018.01.078

[42] Su M, Wang H, Hao H. Axial and radial compressive properties of alumina-aluminum matrix syntactic foam filled thin-walled tubes. Compos. Struct. 2019;226.

https://doi.org/10.1016/j.compstruct.2019.111197

[43] Chollet P. Recent progress in the metallurgy of wrought-zinc alloys. Canadian Metallurgical Quarterly. 2013;7:177-85. https://doi.org/10.1179/cmq.1968.7.3.177

[44] McLean D. The amorphous alloy. Nature. 1955;175:1083. https://doi.org/ 10.1038/1751083a0